HAL
open science

Strongly induced collapse in the Class 0 protostar NGC 1333 IRAS 4A

Arnaud Belloche, Patrick Hennebelle, Philippe André

To cite this version:

Arnaud Belloche, Patrick Hennebelle, Philippe André. Strongly induced collapse in the Class 0 protostar NGC 1333 IRAS 4A. Astronomy and Astrophysics - A&A, 2006, 453, pp.145-154. 10.1051/0004-6361:20054770 . hal-03784963

HAL Id: hal-03784963

https://hal.science/hal-03784963v1

Submitted on 30 Sep 2022

HAL is a multi-disciplinary open access archive for the deposit and dissemination of scientific research documents, whether they are published or not. The documents may come from teaching and research institutions in France or abroad, or from public or private research centers.

L'archive ouverte pluridisciplinaire **HAL**, est destinée au dépôt et à la diffusion de documents scientifiques de niveau recherche, publiés ou non, émanant des établissements d'enseignement et de recherche français ou étrangers, des laboratoires publics ou privés.

A&A 453, 145–154 (2006)
DOI: 10.1051/0004-6361:20054770
© ESO 2006

Astronomy & Astrophysics

Strongly induced collapse in the Class 0 protostar NGC 1333 IRAS 4A

A. Belloche[1], P. Hennebelle[2], and P. André[3,4]

[1] Max-Planck-Institut für Radioastronomie, Auf dem Hügel 69, 53121 Bonn, Germany
e-mail: belloche@mpifr-bonn.mpg.de
[2] LERMA/LRA, École Normale Supérieure, 24 rue Lhomond, 75231 Paris Cedex 05, France
e-mail: patrick.hennebelle@ens.fr
[3] Service d'Astrophysique, CEA/DSM/DAPNIA, C.E. Saclay, 91191 Gif-sur-Yvette Cedex, France
e-mail: pandre@cea.fr
[4] AIM, Unité Mixte de Recherche CEA-CNRS, Université Paris VII, UMR 7158, France

Received 23 December 2005 / Accepted 21 February 2006

ABSTRACT

Context. The onset of gravitational collapse in cluster-forming clouds is still poorly known.
Aims. Our goal is to use the Class 0 protostar IRAS 4A, which is undergoing collapse in the active molecular cloud NGC 1333, to set constraints on this process. In particular we want to measure the mass infall rate and investigate whether the collapse could have been triggered by a strong external perturbation.
Methods. We analyze existing continuum observations to derive the density structure of the envelope, and use our new molecular line observations with the IRAM 30 m telescope to probe its velocity structure. We perform a detailed comparison of this set of data with a numerical model of collapse triggered by a fast external compression.
Results. Both the density and velocity structures of the envelope can be well fitted by this model of collapse induced by a fast external compression for a time of $1-2 \times 10^4$ yr after the formation of the central protostar. We deduce a high mass infall rate of $0.7-2 \times 10^{-4}$ $M_\odot$ yr^{-1}. The momentum required for the perturbation to produce this high mass infall rate is on the same order as the momenta measured for the NGC 1333 numerous outflows. Our analysis also shows that the turbulence is highly non uniform in the envelope, dropping from supersonic to subsonic values toward the center. The inner subsonic turbulence is most likely a relic of the conditions prevailing in the dense core before the onset of collapse.
Conclusions. The vigorous collapse undergone by IRAS 4A was triggered by a fast external compression, probably related to the expansion of a nearby cavity, which could have simultaneously triggered the collapse of the nearby Class 0 protostar IRAS 4B. This cavity could have been generated by an outflow but we have not found a good protostellar candidate yet.

Key words. stars: formation – stars: circumstellar matter – ISM: individual objects: NGC 1333 IRAS 4 – ISM : kinematics and dynamics

1. Introduction

While the first phases of protostellar collapse in distributed star-forming regions like the Taurus molecular cloud start to be observationally better constrained (e.g. Tafalla et al. 1998; Onishi et al. 1999; Motte & André 2001; Belloche et al. 2002), little is known still about the onset of gravitational collapse in cluster-forming clouds where this process is likely to be more violent (see André et al. 2004).

The protostar IRAS 4A is located in the active molecular cloud NGC 1333 that is forming low- and intermediate-mass stars in the Perseus complex (e.g. Sandell & Knee 2001). The NGC 1333 region contains a double cluster of infrared sources, which is one of the least evolved embedded clusters known so far, with an age of $1-2 \times 10^6$ yr (Lada et al. 1996; Lada & Lada 2003). It also contains a population of younger stellar objects, including a few Class 0 protostars (e.g. Looney et al. 2000). IRAS 4A is one of these Class 0 protostars (André et al. 1993). It harbors a 1.8″ binary system at a position angle PA of −50° (Reipurth et al. 2002) and is located in the vicinity of another young multiple system, IRAS 4B (Lay et al. 1995). Both sources are associated with molecular outflows oriented approximately in the north/south direction on a 10″-scale (e.g. Choi 2001, 2005). On a larger scale, the IRAS 4A outflow has a PA ∼ 45° (e.g. Blake et al. 1995). The whole region is actually filled with about ten molecular outflows driven by young protostars that belong to the NGC 1333 protocluster (e.g. Knee & Sandell 2000).

IRAS 4A was identified as a good infall candidate in the surveys of Mardones et al. (1997) and Gregersen et al. (1997). Di Francesco et al. (2001) used the IRAM Plateau de Bure interferometer to probe the inner parts of its envelope. They detected inverse P-Cygni profiles in $H_2CO(3_{12}–2_{11})$ and CS(3–2), which they interpret as infall motions. They derived a high mass infall rate of 1.1×10^{-4} $M_\odot$ yr^{-1}, which is about 70 times higher than the standard accretion rate $\frac{c_s^3}{G}$ at 10 K (Shu 1977). Such a high mass infall rate, if confirmed, cannot occur in an envelope collapsing spontaneously. The collapse of the IRAS 4A envelope was therefore probably triggered by a strong external perturbation. Several authors already argue that the numerous outflows have created cavities affecting the density structure of the molecular cloud and eventually triggered further star formation (Warin et al. 1996; Lefloch et al. 1998; Knee & Sandell 2000; Quillen et al. 2005). In this respect, Sandell & Knee (2001) propose that NGC 1333 is "an example of self-regulated star formation".

Article published by EDP Sciences and available at http://www.edpsciences.org/aa or http://dx.doi.org/10.1051/0004-6361:20054770

However, it still remains to be shown that a collapse triggered by an external perturbation can match the density and velocity structure of a protostellar envelope such as IRAS 4A. This is the purpose of this work. The layout of the paper is as follows. Section 2 summarizes observational details. In Sect. 3 we derive the density structure of the envelope from a compilation of existing continuum data and interpret in terms of velocity structure our new molecular line observations done with the IRAM 30 m telescope. We compare these results in Sect. 4 to radiative transfer models of hydrodynamical simulations of collapse triggered by a fast increase in the external pressure (Hennebelle et al. 2003, 2004). Finally we discuss the implications in terms of triggered star formation in Sect. 5.

2. Observations

We carried out millimeter line observations with the IRAM 30 m telescope at Pico Veleta, Spain, in September and October 2001, and in August 2004, in the following molecular transitions: HCO^+(1–0), $H^{13}CO^+$(1–0), $HC^{18}O^+$(1–0), N_2H^+(1–0), CS(2–1), $C^{34}S$(2–1), HCN(1–0) at 3 mm, CS(3–2), $C^{34}S$(3–2), N_2D^+(2–1) at 2 mm, $H_2CO(3_{12}–2_{11})$, $H_2^{13}CO(3_{12}–2_{11})$, CS(5–4), N_2D^+(3–2) at 1.3 mm, and HCO^+(3–2), $H^{13}CO^+$(3–2) at 1 mm. The references to the frequencies we used are given in Sect. 3.2. The half-power beamwidths can be computed with the equation $HPBW\ ('') = \frac{2460}{\nu(\mathrm{GHz})}$. We used four SIS heterodyne receivers simultaneously and an autocorrelation spectrometer as backend. The spectral resolution was 20 kHz at 3 mm and 2 mm, and 40 kHz at 1.3 mm and 1 mm in 2001, and 10 kHz at 3 mm and 20 kHz at 1.3 mm in 2004. The observations were done in single-sideband mode with sideband rejections of 0.01 at 3 mm and 0.05 at 2, 1.3, and 1 mm. Accordingly, the calibration uncertainty was ~10%. The forward efficiencies F_{eff} were 0.95 at 3 mm, 0.93 at 2 mm, 0.91 at 1.3 mm, and 0.88 at 1 mm. The main-beam efficiencies were computed using the Ruze function $B_{\mathrm{eff}} = 1.2\epsilon\ \mathrm{e}^{-(4\pi R\sigma/\lambda)^2}$, with $\epsilon = 0.69$, $R\sigma = 0.07$, and λ the wavelength in mm. The system temperatures ranged from ~110 K to ~160 K at 3 mm, ~190 K to ~250 K at 2 mm, ~320 K to ~670 K at 1.3 mm, and ~550 K to ~1200 K at 1 mm. The telescope pointing was checked every ~2 h on Saturn, 3C 84, and/or NRAO 140, and found to be accurate to 3″ (rms). The telescope focus was optimized on Saturn and/or 3C 84 every ~3 h. Position-switching and on-the-fly observations were done with a reference position located at either (3000″, 3000″), (1500″, 1500″), (0″, −240″), or (150″, 120″) relative to the envelope center $\alpha_{\mathrm{J2000}} = 03^{\mathrm{h}}29^{\mathrm{m}}10\overset{\mathrm{s}}{.}30$, $\delta_{\mathrm{J2000}} = 31°13'31.8''$, as measured in the 1.3 mm emission by Motte & André (2001)[1]. The data were reduced with the CLASS software package (Buisson et al. 2002). The spectra were converted from antenna temperature to main-beam temperature using the equation $T_{\mathrm{mb}} = \frac{F_{\mathrm{eff}}}{B_{\mathrm{eff}}} T_{\mathrm{a}}^*$.

In addition, we downloaded from the JCMT archive CS(5–4), CS(7–6), $C^{34}S$(5–4), HCO^+(4–3), $H^{13}CO^+$(3–2), and DCO^+(5–4) spectra observed toward IRAS 4A in February and July 1992, February 1994, November 1999, and October 2001. The data were converted into fits files with SPECX (Padman 1993; Matthews & Jenness 1997), reduced with CLASS and converted to main-beam temperatures using beam efficiencies $\eta_{\mathrm{mb}} = 0.69$ at 1 mm and 0.63 at 0.85 mm (see Maret et al. 2004, for the conversion to T_{mb} at JCMT).

[1] Note that our central position is offset from the two components observed by Reipurth et al. (2002) with VLA by 3″ and 1.5″ toward the West.

Table 1. Interferometric measurements of dust continuum emission.

Ref.[(1)]	λ (mm)	*HPBW* (″ × ″)	$F_{\mathrm{peak}}^{(2)}$ (mJy beam^{-1})	$F_{\mathrm{int}}^{(3)}$ (mJy)	Size (″ × ″)	Interf.
D01	1.33	2.0 × 1.7	1200 ± 16	3100 ± 470	5.3 × 4.1	PdBI
D01	2.04	3.2 × 2.3	450 ± 14	690 ± 110	4.4 × 3.4	NMA
D01	2.19	3.4 × 2.6	420 ± 10	580 ± 90	4.2 × 3.3	NMA
L00	2.7	5.5 × 5.0	351 ± 3	544 ± 14	25 × 24	BIMA
		3.0 × 2.8	280 ± 2	526 ± 9	12 × 18.5	BIMA
		1.2 × 1.1	172 ± 2	450 ± 10	5.4 × 6.2	BIMA
D01	3.22	2.9 × 2.6	200 ± 4.4	320 ± 49	4.5 × 3.7	PdBI
D01	6.92	2.1 × 1.9	16 ± 0.29	26 ± 4	3.3 × 2.8	VLA
D01	13.3	3.8 × 3.1	3.1 ± 0.27	4.7 ± 1.0	6.3 × 3.6	VLA

[(1)] References: L00: Looney et al. (2000); D01: Di Francesco et al. (2001). [(2)] Quoted errors are statistical only and do not include any systematic calibration uncertainties. [(3)] Flux integrated over a region of size listed in Col. 6.

Table 2. Single-dish measurements of dust continuum emission.

Ref.[(1)]	λ (mm)	*HPBW* (″)	$F_{\mathrm{peak}}^{(2)}$ (Jy beam^{-1})	$F_{\mathrm{int}}^{(3)}$ (Jy)	Size (″ × ″)	Telescope
S00	0.85	16.0	10.30 ± 0.03	12.9	30 × 23	SCUBA
S01	0.85	14.0	...	9.05	14.2 × 5.4	SCUBA
L98	1.25	11.0	3.10 ± 0.01	4.7	18.8 × 18.8	30 m
M01	1.25	11.5	4.10 ± 0.02	4.1	24 × 24	30 m
				7.3	97 × 97	30 m

[(1)] References: L98: Lefloch et al. (1998); S00: Smith et al. (2000); S01: Sandell & Knee (2001); M01: Motte & André (2001). [(2)] Quoted errors are statistical only and do not include any systematic calibration uncertainties. [(3)] Flux integrated over a region of size listed in Col. 6.

3. Results

3.1. Continuum emission

The mass distribution of the IRAS 4A envelope can be estimated from the dust continuum emission. From the literature we compiled the interferometric (Table 1) and single-dish (Table 2) measurements done so far. Masses were estimated by various authors using different assumptions for the dust emissivity, the dust temperature distribution, and/or the distance to NGC 1333. Here, we analyze this set of data homogeneously. We assume a distance of 318 pc, based on the *Hipparcos* parallactic measurements of the Perseus OB2 association (de Zeeuw et al. 1999), as discussed by Getman et al. (2002). With this distance, the bolometric luminosity derived by Sandell et al. (1991) becomes 11.6 $L_\odot$. We use a dust emissivity $\kappa_\lambda = 0.1 \times (\lambda/250\ \mu\mathrm{m})^{-\beta}$ cm^2 g^{-1} (Hildebrand 1983). The dust temperature profile is assumed to be fixed by the heating by the central protostar as suggested by Terebey et al. (1993):

$$T_{\mathrm{d}}(r) = 25 \left(\frac{r}{6684\ \mathrm{AU}}\right)^{-q} \left(\frac{L}{520\ L_\odot}\right)^{q/2}, \quad (1)$$

with $q = 2/(4+\beta)$ and $L = 11.6\ L_\odot$. We compute the mass within a spherical radius R assuming optically thin emission and a temperature equal to $T_{\mathrm{d}}(R)$. However, this calculation overestimates the true mass because of the radius dependence of the temperature. When the temperature and the density are single power laws with slopes $-q$ and $-p$, respectively, and the Rayleigh-Jeans approximation is valid, the correction factor is $(1 - \frac{q}{3-p})$. For radii smaller than ~9200 AU, $T_{\mathrm{d}}(r) > 10$ K and this approximation should be valid, provided the density profile follows a power

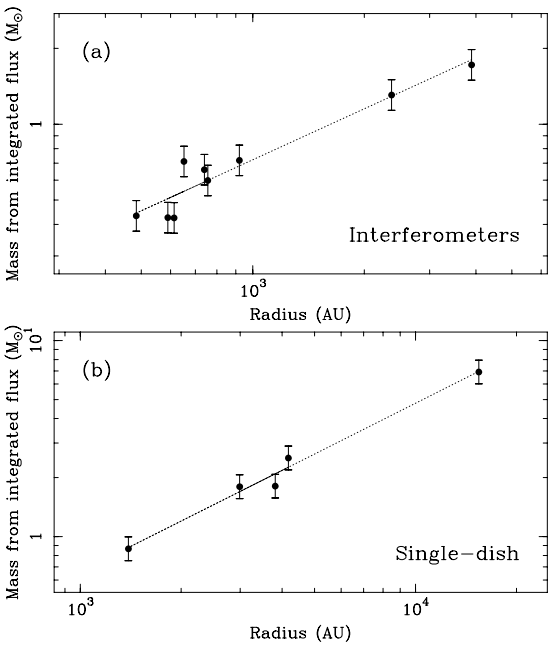

Fig. 1. Mass distribution estimated from the integrated flux of continuum emission measured with **a)** interferometers (see Table 1) and **b)** single-dish telescopes (see Table 2), and computed using the best-fit opacity exponent $\beta = 0.85$.

law. For larger radii, we expect the dust grains to also be heated by the external UV radiation field via the photoelectric effect (e.g. Lesaffre et al. 2005). For simplicity, we assume that the dust temperature stays at 10 K for a radius larger than 9200 AU. In this case, the correction factor to compute the mass within a radius $R > 9200$ AU is

$$\left(\frac{q}{3-p-q} \times \left(\frac{R_1}{R}\right)^{3-p} + 1\right)^{-1}, \quad (2)$$

where R_1 (~9200 AU) is the radius where the temperature starts to be constant.

Given these assumptions, the emissivity exponent minimizing the mass dispersion of the interferometric measurements shown in Fig. 1a is $\beta = 0.85 \pm 0.15$, yielding $\kappa_{1.3\,\mathrm{mm}} = 0.025 \pm 0.006$ cm^2 g^{-1}. At larger radii with the single-dish measurements, we get $\beta = 1.1 \pm 0.6$, which is poorly constrained because these measurements are not spread out enough in wavelength. In the following, we use $\beta = 0.85$. The best power-law fits to the masses derived from the interferometric and single-dish measurements are $M(r) = 1.9 \times (r/4200\,\mathrm{AU})^{0.67}\ M_\odot$ and $M(r) = 3.1 \times (r/4200\,\mathrm{AU})^{0.86}\ M_\odot$, respectively (see Fig. 1). A fit to all the data gives $M(r) = 2.7 \times (r/4200\,\mathrm{AU})^{0.77}\ M_\odot$. For comparison, the mass of the singular isothermal sphere enclosed in 4200 AU at 10 K is only 0.34 $M_\odot$. We note that the interferometric measurements should resolve out any extended emission from the environment, and therefore give a more reliable estimate of the mass distribution within 13″ in the IRAS 4A envelope.

Assuming a spherical geometry and a power-law density profile $n_{\mathrm{H_2}} = n_0(\frac{r}{r_0})^{-p}$, the fit to the interferometric mass measurements yields $p = 2.3$ and $n_0 = 2.1 \times 10^5$ cm^{-3} at $r_0 = 4200$ AU. By analyzing their 2.7 mm interferometric measurements, Looney et al. (2003) found no evidence of a circumstellar disk and they measured a power-law index p between 1.7 and 2.3, which is consistent with our result (see their Table 1). Note also that n_0 is 4 times higher than the density of a singular isothermal sphere at 10 K, and this ratio is even higher at smaller radii.

3.2. Spectroscopic signature of collapse

In Fig. 2 we compare the CS, $C^{34}S$, N_2H^+, HCO^+, $H^{13}CO^+$, and $HC^{18}O^+$ spectra that we obtained toward the central position of IRAS 4A with the IRAM 30 m telescope, as well as CS, $C^{34}S$, HCO^+, $H^{13}CO^+$, and DCO^+ spectra that we took from the JCMT archive. Among the latter, CS(5–4) and CS(7–6) were observed at a position that is slightly offset in right ascension (less than 3″). We used the CS and $C^{34}S$ frequencies measured by Gottlieb et al. (2003), the N_2H^+(1–0) frequency determined by Dore et al. (2004), the DCO^+ frequencies measured by Caselli & Dore (2005), the HCO^+ frequencies from the CDMS database (as of October 2005, Müller et al. 2005), and the $H^{13}CO^+$ and $HC^{18}O^+$ frequencies determined by Schmid-Burgk et al. (2004).

The spectra of Fig. 2 show the classical signature of collapse, namely self-absorbed optically thick lines, with the blue peak stronger than the red one, and low-optical-depth spectra peaking in between (see Evans 1999; Myers et al. 2000). This signature is seen at 20″ in the east/west direction in our HCO^+(3–2) map, but is only seen on the central position in our CS(5–4) map with a 10″ spacing. Since the smoothing of our CS(5–4) map to the JCMT resolution yields a very similar spectrum to the JCMT one, the infall signature seen in the JCMT spectrum comes entirely from the inner 10″ probed by the IRAM 30 m telescope.

In the classical spectroscopic signature of collapse motions (Evans 1999), the shift of the dip of the optically thick lines with respect to the systemic velocity of the source given by the centroid velocity of an optically thin line is an indication of the infall velocity of the absorbing material. A fit to the hyperfine multiplet of N_2H^+(1–0) yields a low optical depth of 0.33 ± 0.02 for the isolated component 101–012, and a centroid velocity $V_{\mathrm{N_2H^+}} = 7.24 \pm 0.01$ km s^{-1}, which we take as the systemic velocity of the source. With respect to this systemic velocity, we measure shifts of 0.4, 0.4, and 0.5 km s^{-1} for CS(2–1), (3–2), and (5–4), respectively, and shifts of 0.5 and 0.5 km s^{-1} for HCO^+(3–2) and (4–3), respectively, all measured with an uncertainty of 0.1 km s^{-1}. Di Francesco et al. (2001) measured a self-absorption at 7.64 km s^{-1} with the Plateau de Bure interferometer in $H_2CO(3_{12}–2_{11})$, i.e. at the same velocity as the self-absorption in our CS(2–1) spectrum.

The $C^{34}S$(2–1) and (3–2) spectra are also asymmetric, with even a marked dip for $C^{34}S$(2–1). These lines could be optically thick and self-absorbed, like the CS lines. On the other hand, they could be optically thin but probe two velocity components along the line of sight. This would be the case for an infalling envelope with strong depletion at the center (see the case of L1544 in Caselli et al. 2002), or with a small non-thermal velocity dispersion compared to the infall velocities, or for two independent velocity components, one being physically unrelated to the envelope. We address this question in Sects. 4 and 5. With a signal-to-noise ratio of 3, only one peak is detected in the JCMT $C^{34}S$(5–4) spectrum, at the same velocity as the $C^{34}S$(2–1) blue component.

3.3. Extended wings tracing the outflow

In Fig. 3 we present contour maps of the CS(2–1) and CS(5–4) line-wing emission overlaid on the intensity maps of the line core. Both show a clear bipolar morphology whose direction

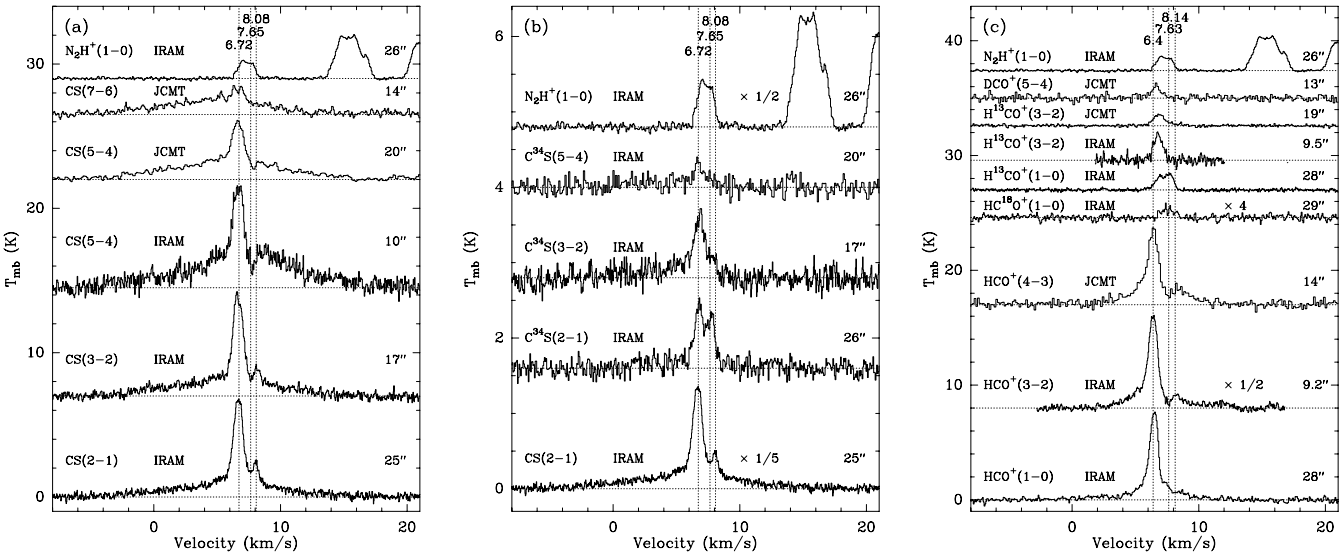

Fig. 2. Spectra toward the center of the IRAS 4A envelope obtained with the 30 m telescope or taken from the JCMT archive: **a)** CS and N_2H^+ spectra, **b)** $C^{34}S$ spectra along with CS(2–1) and N_2H^+(1–0), **c)** HCO^+, $H^{13}CO^+$, $HC^{18}O^+$, and DCO^+ spectra along with N_2H^+(1–0). The vertical dotted lines show the position of the blue peak, the red peak, and the dip of the CS(2–1) spectrum in **a)** and **b)**, and the same for HCO^+(3–2) in **c)**. The temperature scale is in T_{mb}. The beamwidth (*HPBW*) is given for each spectrum.

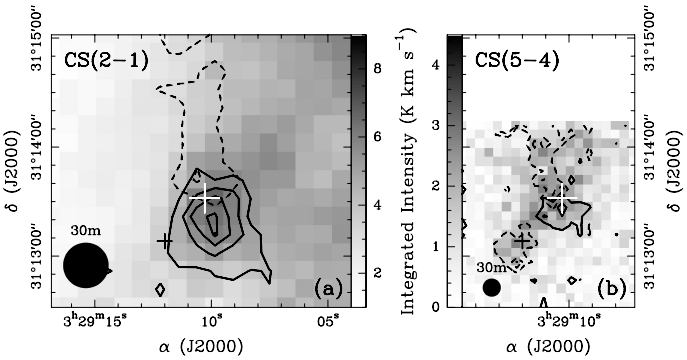

Fig. 3. a) CS(2–1) intensity maps toward IRAS 4A integrated over [−4.10, 5.91] km s^{-1} (*thick contours*), [6.06, 8.31] km s^{-1} (*grey scale*), and [8.46, 15.50] km s^{-1} (*dashed contours*). The contours go from 1.5 to 6 by 1.5 and from 1.5 to 3 by 1.5 K km s^{-1}, respectively. **b)** CS(5–4) intensity maps integrated over [−1.37, 5.91] km s^{-1} (*thick contours*), [6.26, 8.11] km s^{-1} (*grey scale*), and [8.46, 12.00] km s^{-1} (*dashed contours*). The contours are 2 and 4, and 0.7 and 1.4 K km s^{-1}, respectively. The intensity scale is $T_a^\star$. The IRAM 30 m beam size is shown in each panel (*HPBW*). The big/white and small/black crosses mark the positions of IRAS 4A and IRAS 4B, respectively.

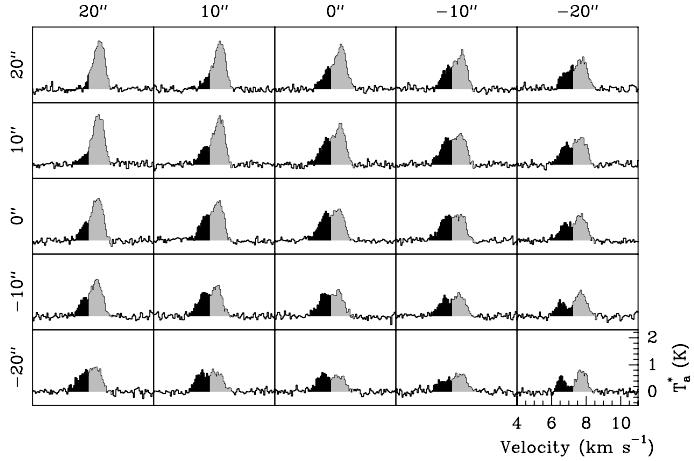

Fig. 4. Map of $H^{13}CO^+$(1–0) spectra taken toward IRAS 4A with the IRAM 30 m telescope. Each spectrum is divided into two components, filled in black for $v < 7.30$ km s^{-1} and in grey for $v > 7.30$ km s^{-1}. The half-power beam width is 28″.

PA ∼ 10° matches the direction of the outflow known in this source on a small scale (see Sect. 1). The wings of the CS (and HCO^+) central spectra in Fig. 2 are thus certainly associated with the molecular outflow. They extend to higher velocities in CS (from $v = -2$ to 15 km s^{-1}) than in HCO^+ (3 to 11 km s^{-1}).

3.4. Maps of low optical depth tracers

Figure 4 shows a map of $H^{13}CO^+$(1–0) spectra taken toward IRAS 4A with the IRAM 30 m telescope. Nearly all spectra are double-peaked, as are our $C^{34}S$ spectra with a slightly worse signal-to-noise ratio. The intensity of the blueshifted component peaks at the IRAS 4A central position, this behavior being more pronounced in the northeast/southwest direction than in the perpendicular direction. This component is thus certainly physically associated with the IRAS 4A envelope. By fitting two Gaussian components to each spectrum, we measure for the blueshifted component a centroid velocity gradient of ∼9.7 km s^{-1} pc^{-1} with a position angle PA = 38° from North to East. On the other hand, the intensity of the redshifted component increases from the South-West to the North-East, and shows only a small velocity gradient of 2.4 km s^{-1} pc^{-1} at PA = 7°. The interpretation of these velocity gradients in terms of rotation is not straightforward.

In Fig. 5 we present large-scale maps of N_2H^+(101–012) intensity integrated over the same velocity ranges as for $H^{13}CO^+$(1–0) above (see Fig. 4). First of all, we notice that the N_2H^+(101–012) emission has a local maximum very close to IRAS 4A in both Figs. 5a and b, which strongly suggests that *both* the blueshifted and redshifted components are related to the protostar. Second, these maps show that the N_2H^+(101–012) emission traces the same structure as the dust continuum emission (e.g. Sandell & Knee 2001; Hatchell et al. 2005): a filamentary structure extending along a direction with a position angle

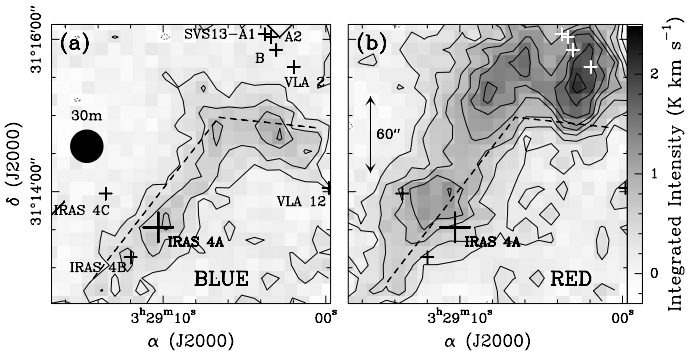

Fig. 5. Maps of N_2H^+(101–012) intensity integrated over **a)** the blueshifted velocity range [5.95, 7.30] km s^{-1} and **b)** the redshifted velocity range [7.30, 8.65] km s^{-1}, observed with the IRAM 30 m telescope (*HPBW* 26″, shown on the left). The first contour and contour step are 0.25 K km s^{-1} on $T_a^\star$ scale on both maps. The big cross marks the central position we used for IRAS 4A. The small crosses mark the positions of the VLA and BIMA continuum sources observed by Reipurth et al. (2002) and Looney et al. (2000). The dashed line separates the two components. It emphasizes the spatial shift between them and their shell-like structure.

PA ∼ −45°, which bends at PA ∼ −90° in the West. Furthermore, these maps provide additional kinematical information and show that the two components that we identified in $H^{13}CO^+$(1–0) have the same morphology but are spatially shifted: the "blue" filament is shifted by ∼30″ toward the South-West with respect to the "red" filament. Since they share the same morphology, they are likely to be physically related and not overlap by chance along the line of sight.

4. Comparison to collapse models

The classical signature of infall seen in our CS and HCO^+ observations (see Sect. 3.2 and Fig. 2) suggests that the envelope of IRAS 4A is collapsing, confirming the analysis of Di Francesco et al. (2001). They suggest that the inverse P-Cygni profiles that they observed with the IRAM Plateau de Bure Interferometer toward IRAS 4A in $H_2CO(3_{12}–2_{11})$ are created by an infalling envelope with a mass infall rate of 1.1×10^{-4} $M_\odot$ yr^{-1}. This rate is nearly two orders of magnitude higher than the standard accretion rate $\frac{c_s^3}{G}$ at 10 K (Shu 1977), and is the result of both higher densities and velocities (see Sects. 1 and 3.1). It is thus very unlikely that the collapse of this protostellar envelope has occurred spontaneously, so we investigate models of collapse induced by a fast external compression in this section.

4.1. Model of collapse induced by compression

Hennebelle et al. (2003, 2004) used a smoothed-particle-hydrodynamics code to investigate the collapse of prestellar and protostellar cores driven from the outside by an increase in the external pressure. In the following, we compare our observations to their non-rotating model with rapid compression, i.e. $\phi = 0.03$, where ϕ is the time-scale on which the external pressure doubles divided by the initial sound-crossing time. Such a rapid compression is required to get a density enhancement that matches the density profile of the IRAS 4A envelope (see Sect. 4.2). On the other hand, a more rapid compression produces infall velocities that are too high to get a good agreement with our observations toward IRAS 4A. The initial conditions of the model correspond to a core in stable hydrostatic equilibrium.

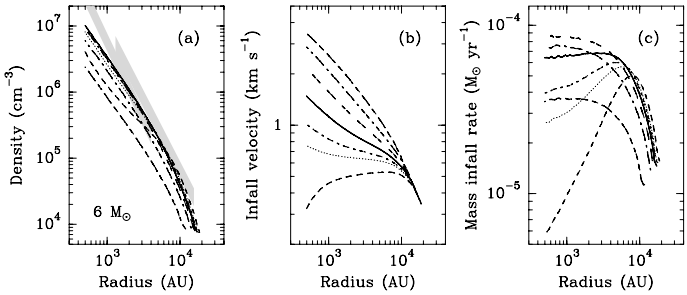

Fig. 6. a) Density, **b)** infall velocity, and **c)** mass infall rate profiles of the collapse model induced by compression described in Sect. 4.1 at times 0.8402, 0.8533, 0.8581, 0.8657, 0.8763, 0.8920, and 0.9249×10^6 yr, corresponding to renormalized times after the formation of the central protostar of approximately −7, 7, 11, 19, 30, 45, and 78×10^3 yr, respectively. The thick line corresponds to 1.9×10^4 yr and indicates the "best-fit" model used in Sect. 4.3 and shown in Fig. 7. The dashed areas in (a) show the constraints deduced for IRAS 4A from the interferometric and single-dish continuum measurements (see Sect. 3.1).

It is embedded in a hot rarefied external medium and has the structure of a Bonnor-Ebert sphere with a dimensionless radius $\xi_b = 3$, i.e. smaller than the dimensionless radius $\xi_b = 6.45$ of the critical Bonnor-Ebert sphere (e.g. Bonnor 1956). We normalized the model to a kinetic temperature of 10 K and a total mass of 6.0 $M_\odot$.

4.2. Mass distribution

Figure 6a compares the evolution of the density profile of the model described in Sect. 4.1 with the density profiles deduced from the interferometric and single-dish continuum measurements toward IRAS 4A in Sect. 3.1. The fast external compression is responsible for a significant increase in the density profile compared to the profile expected for a singular isothermal sphere. The agreement with the profiles deduced from the observations is good in the range 1500–10 000 AU at times $1–3 \times 10^4$ yr after the formation of the central point mass, which are on the same order as the estimated lifetime of Class 0 protostars (André et al. 2000). The disagreement at smaller radii, the model being less dense than what we deduced from the observations assuming spherical symmetry, could be due to the presence of an unresolved disk not removed from the interferometric fluxes analyzed in Sect. 3.1. However, Looney et al. (2003) did not find any evidence of such a disk. At larger radii, the single-dish measurements might be contaminated by large-scale emission from the cloud along the line of sight, which is not related to the protostellar envelope itself, although the dual-beam technique used for the observations should have removed most of it.

4.3. Radiative transfer modeling

We used the Monte-Carlo-based radiative transfer code MAPYSO in one spherical dimension (see Blinder 1997; Belloche et al. 2002) to compute the CS, $C^{34}S$, and N_2H^+ spectra that would be observed for a source set in collapse by fast compression, as described by the model of Sect. 4.1. In addition to the density and velocity profiles of the hydrodynamical model at time 1.9×10^4 yr (see Figs. 6 and 7a, e), we used a uniform $CS/C^{34}S$ isotopic ratio of 22.5 but non-uniform abundance profiles (see Fig. 7c). For N_2H^+, we used the collision rates of HCO^+ with H_2 (Flower 1999) and assumed a constant abundance of 4.1×10^{-10}. We did not model the hyperfine

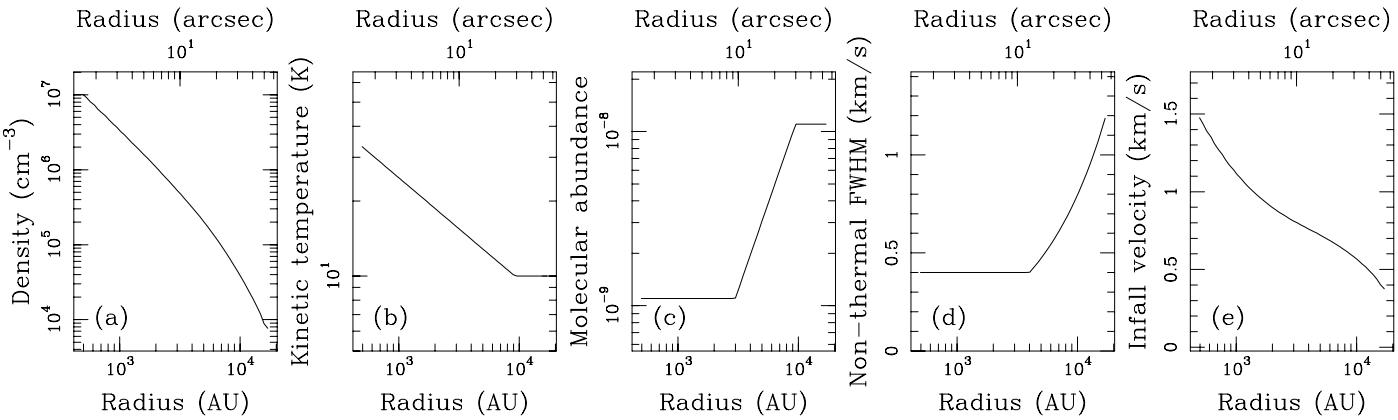

Fig. 7. a) Density, **b)** kinetic temperature, **c)** CS molecular abundance, **d)** non-thermal line broadening (FWHM), and **e)** infall velocity profiles of the collapse model at time 1.9×10^4 yr used for the radiative transfer modeling of Fig. 8.

structure but simply rescaled the abundance effectively used for the calculations by the statistical weight ratio $\frac{3}{27}$ and fitted only the 101–012 optically thin component. For all molecules, we added a *non-uniform* non-thermal line broadening to the thermal broadening (see Fig. 7d). Although the hydrodynamical simulation was isothermal, we used a non-uniform kinetic temperature to compute the spectra, which are very sensitive to the heating by the central protostar. The temperature was set to the dust temperature profile described in Sect. 3.1 (see Fig. 7b).

In Fig. 8 we compare the synthetic spectra at time 1.9×10^4 yr to the spectra observed toward IRAS 4A along the longitude axis, i.e. roughly perpendicular to the outflow axis (see Fig. 3). The asymmetry and the absorption dips of the central CS(2–1) and CS(3–2) spectra are well reproduced. The asymmetry of these optically thick lines is enhanced toward the West and reduced toward the East at ±20″, which is not accounted for by our 1D spherical model. However, including some rotation could improve the modeled spectra in that respect (see Belloche et al. 2002, for such an effect in IRAM 04191+1522 – hereafter IRAM 04191). The line wings are not reproduced by our model, which was expected since they trace the ouflow that we did not include in our modeling (see Sect. 3.3). The relative contribution of the outflow gets stronger with the upper energy level of the transition, and even masks the red peak of the CS(5–4) spectrum. This spectrum is reasonably well-matched by the model, although the shape of the dip is not reproduced fully.

The central $C^{34}S$(2–1) modeled spectrum matches the observed one well. It is optically thin ($\tau = 0.4$) and the two peaks result from the large infall velocities dominating the non-thermal line broadening in the inner parts of the envelope. We emphasize the importance of modeling the optically thin lines of a less abundant isotopologue *simultaneously* with the optically thick lines of the main molecule. This indeed reduces the space of free parameters drastically – especially the non-thermal line broadening and the abundance – and helps in deriving reliable infall velocities from the optically-thick, self-absorbed, asymmetric spectra. In particular, a first strong constraint is set on the abundance profile by the spatial variations of the $C^{34}S$(2–1) integrated intensity, which imply a decrease in the abundance toward the center. Besides, a second constraint on the abundance in the external parts comes from the depth of the absorption dips of the CS(2–1) and CS(3–2) lines. As a result, this set of data reveals that CS is strongly affected by depletion in the IRAS 4A envelope (see Belloche et al. 2002, for a similar result in the Class 0 protostar IRAM 04191).

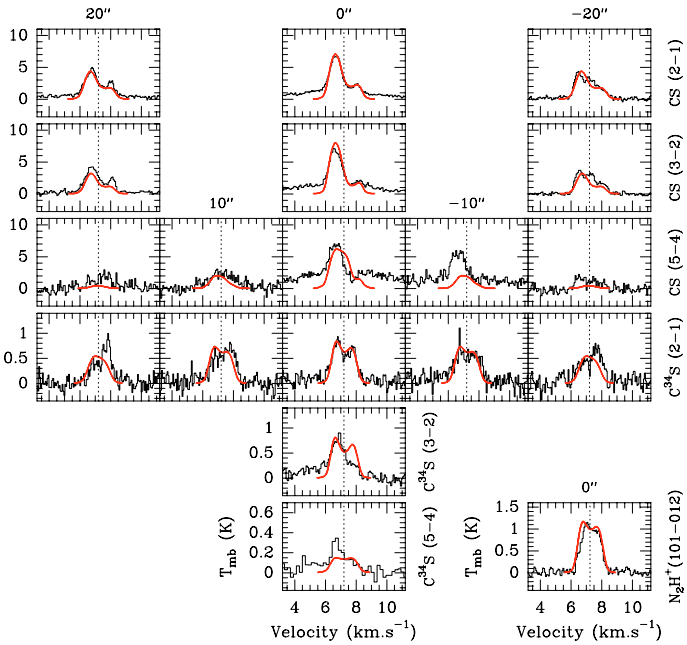

Fig. 8. CS, $C^{34}S$, and N_2H^+ spectra (*histograms*) in units of main-beam temperature observed toward IRAS 4A along the longitude axis (see references in Fig. 2). Synthetic spectra corresponding to the collapse model at time 1.9×10^4 yr described in Sect. 4.1 are superimposed (*red/thick line*). The dotted line indicates the envelope systemic velocity used for the computation of the radiative transfer (7.20 km s^{-1} for CS and $C^{34}S$, and 7.24 km s^{-1} for N_2H^+).

The N_2H^+(101–012) line is also well reproduced, although the observed blue peak is not as blueshifted as in the model. The opacity of the modeled spectrum is 0.24. It agrees reasonably well with the opacity obtained from the Gaussian fit to the hyperfine structure (see Sect. 3.2), and this small discrepancy may be due to our simplified treatment of the radiative transfer of N_2H^+. With the uniform abundance, the N_2H^+(1–0) transition is more sensitive to the inner region than the $C^{34}S$(2–1) line. We tried a model that included depletion of N_2H^+ above $\sim 10^6$ cm^{-3} (see Belloche & André 2004, for N_2H^+ depletion in IRAM 04191), but the shape of the line was worse, the blue and red peaks being much more pronounced than they are in the observed spectrum. The reason the uniform abundance produces a profile with less pronounced blue and red peaks is that, in this case, the beam picks up more material at low velocities projected along the line

of sight, i.e. the material infalling along a direction close to the plane of the sky. This shows that the double-peaked profile of the $C^{34}S$(2–1) line is due not only to the large infall velocities compared to the non-thermal broadening, as stated above, but also to the depletion in the central region. In our model, the shape of the N_2H^+(101–012) line therefore indicates no depletion of N_2H^+ (or very little) in the inner regions.

As noted above, the non-thermal line broadening in the inner parts of the envelope is strongly constrained to be small ($\Delta V_{\rm NT} \sim 0.4$ km s^{-1}, i.e. $\sigma_{\rm NT} \sim 0.17$ km s^{-1}) by the double-peaked line shape of the low-optical-depth $C^{34}S$(2–1) spectrum. The model with $\Delta V_{\rm NT} = 1.1$ km s^{-1} in Fig. 9 indeed shows that a larger broadening smoothes out the $C^{34}S$(2–1) double-peaked line profile which traces the infall velocities of the front and rear hemispheres. It also broadens the N_2H^+(101–012) spectrum too much and produces wings that have not been observed. On the other hand, the CS(2–1) and (3–2) broad absorption dips require a much larger non-thermal line broadening in the external parts of the envelope where they are produced ($\Delta V_{\rm NT} \sim 1.2$ km s^{-1}, i.e. $\sigma_{\rm NT} \sim 0.5$ km s^{-1}). The model with $\Delta V_{\rm NT} = 0.4$ km s^{-1} in Fig. 9 indeed shows that a smaller broadening cannot produce the broad absorption dips observed in CS(2–1) and CS(3–2). We have, therefore, strong evidence that *the non-thermal line broadening is not uniform* in the IRAS 4A envelope, decreasing by nearly a factor of three toward the center, from supersonic down to subsonic values. This conclusion agrees quite well with the small linewidths $\Delta V_{\rm NT} \sim 0.5$ km s^{-1} observed toward IRAS 4A in N_2H^+(1–0) by Di Francesco et al. (2001) on small scales with PdBI ($r \sim 1000$ AU) and the much larger linewidths $\Delta V_{\rm NT} \sim 1.0$–$1.9$ km s^{-1} measured in the NGC 1333 molecular cloud with the low-density tracer $C^{18}O$(1–0) by Warin et al. (1996).

The time elapsed since the point-mass formation in the collapse model is well constrained by the peak separations and the linewidths of the CS and $C^{34}S$ spectra. The infall velocities of the model at time 7×10^3 yr in Fig. 10 are not high enough to produce the right separation of the peaks of the CS(3–2) and $C^{34}S$(2–1) lines. On the other hand, the much higher infall velocities of the model at time 4.5×10^4 yr produce spectra that are too broad. As a result, we find *a good match for a time of 1–2 $\times10^4$ yr elapsed since the formation of the central protostar*.

Finally, we could not find a better match in the framework of our 1D spherical modeling for the $C^{34}S$(3–2) and $C^{34}S$(5–4) central spectra. The modeled spectra of Fig. 8 are not asymmetric enough for these two lines. Since our modeling suggests low optical depths of 0.35 and 0.04 for these two lines, it is very unlikely that the observed asymmetry results from an optical depth effect. This instead suggests that the material emitting in these two lines at the blue and redshifted velocities – i.e. in the rear and front hemispheres, respectively, in the framework of this collapse model – is denser for the former and less dense for the latter than assumed in the model.

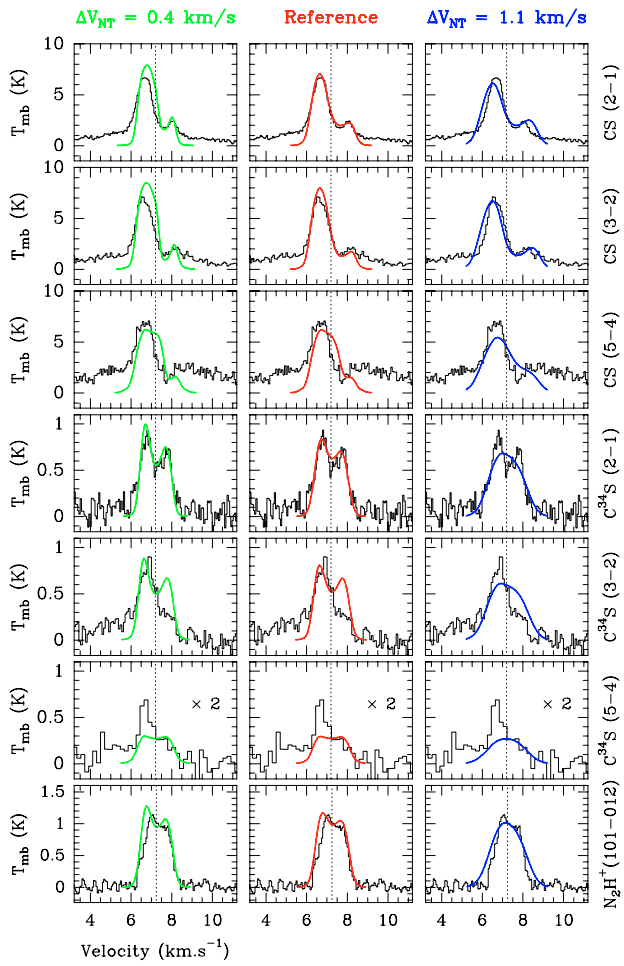

Fig. 9. CS, $C^{34}S$, and N_2H^+ spectra in units of main-beam temperature observed toward the center of IRAS 4A (*histograms*). Each column shows a different model (*thick line*). Synthetic spectra corresponding to the collapse model at time 1.9×10^4 yr described in Sect. 4.1 are superimposed in the central column (*in red*). In the left and right columns, the synthetic spectra (*in green and blue*) were obtained with the same input model, except for the non-thermal broadening, which was in both cases uniform with $\Delta V_{\rm NT} = 0.4$ and 1.1 km s^{-1}, respectively. The dotted line indicates the systemic velocity of the envelope that was used to compute the radiative transfer (see Fig. 8).

5. Discussion

5.1. A vigorous collapse induced by a fast compression

In Sect. 4 we found very good agreement between the continuum and CS/$C^{34}S$/N_2H^+ line observations toward IRAS 4A and the collapse model of Hennebelle et al. (2003) induced by a fast external compression with $\phi = 0.03$. The best match is obtained for a time of 1–2 $\times10^4$ yr elapsed since the formation of the central protostar. This corresponds to a mass infall rate of 4–7 $\times10^{-5}$ $M_\odot$ yr^{-1} in the range of radii [10^3, 10^4] AU (see Fig. 6c). However, the actual mass infall rate is probably even higher since the density profile of our model does not perfectly match (and underestimates it by about 25%) the density profile deduced from the observations (see Fig. 6a). Also, the dust opacity we used in Sect. 3.1 is 2.5 times larger than the opacity usually assumed for protostellar envelopes (e.g. Motte & André 2001). Therefore we estimate that the actual mass infall rate is most probably in the range 0.7–2 $\times10^{-4}$ $M_\odot$ yr^{-1}. This is in very good agreement with the mass infall rate of 1.1×10^{-4} $M_\odot$ yr^{-1} deduced by Di Francesco et al. (2001) from their PdBI observations. As already mentioned in Sect. 4, such a mass infall rate of 1×10^{-4} $M_\odot$ yr^{-1} is 60 times higher than the standard accretion rate $\frac{c_s^3}{G}$ at 10 K (Shu 1977). In our model, it is the result of both higher densities and velocities produced by the fast compression wave propagating inwards. Fatuzzo et al. (2004) find that the mass infall rate indeed scales roughly linearly with the initial overdensity and the initial velocity field in their self-similar collapse solutions where the dense core is initially either overdense

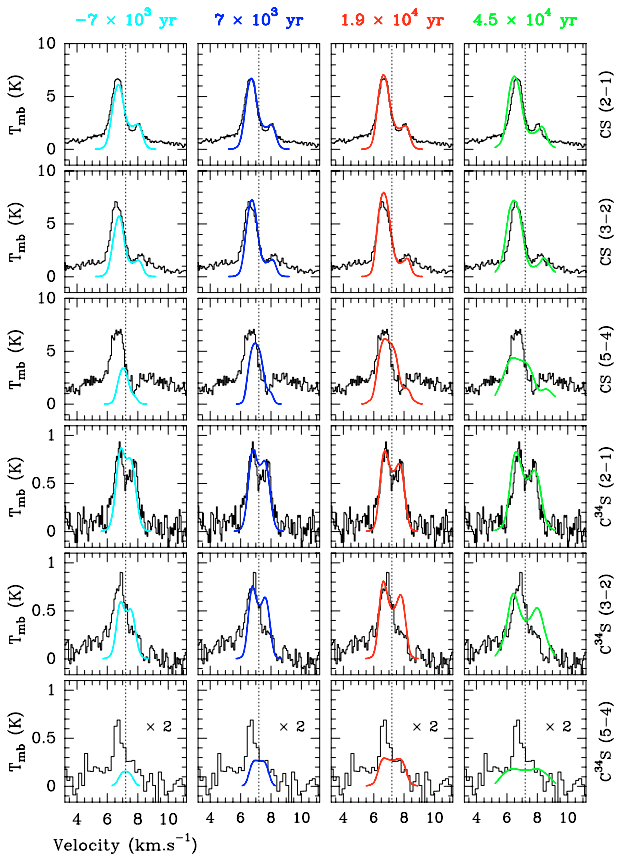

Fig. 10. CS and $C^{34}S$ spectra in units of main-beam temperature observed toward the center of IRAS 4A (*histograms*). Each column shows a different model (*thick line*). Synthetic spectra corresponding to the collapse model described in Sect. 4.1 at times −7, 7, 19, and 45×10^3 yr are superimposed from left to right (*in light blue, blue, red, and green*). For each model, the scaling of the abundance profile was adjusted to match the peak intensity of the $C^{34}S$(2–1) line. The dotted line indicates the systemic velocity of the envelope that was used to compute the radiative transfer (see Fig. 8).

compared to the singular isothermal sphere or has nonzero initial velocities.

In the framework of the self-similar inside-out collapse model with an effective sound speed including a non-thermal contribution, the "standard" accretion rate would be $\frac{(c_s^2+\sigma_{\rm NT}^2)^{3/2}}{G}$ (Shu et al. 1987). This "effective" accretion rate would be at most 3 times higher than the pure isothermal one with the non-thermal velocity dispersion $\sigma_{\rm NT} = 0.17$ km s^{-1} derived for the inner parts of the envelope in Sect. 4.3, which is typical of the level of turbulence in prestellar condensations (e.g. Belloche et al. 2001), but probably even an upper limit for IRAS 4A since the smallest dispersion measured by Di Francesco et al. (2001) with PdBI is 0.09 km s^{-1}. This cannot account for the high mass infall rate measured in the IRAS 4A envelope. On the other hand, the Larson-Penston similarity solution (Larson 1969; Penston 1969) has a uniform mass infall rate of $29 \times \frac{c_s^3}{G}$ at the point-mass formation, and its extension after the point-mass formation by Hunter (1977) has a mass infall rate approaching asymptotically $47 \times \frac{c_s^3}{G}$. This value is closer to our result for IRAS 4A, which is not surprising since the Larson-Penston solution, among the numerous similarity solutions of isothermal gravitational collapse, can be physically interpreted as a model associated with a strong external compression wave (Whitworth & Summers 1985). Similarity solutions are helpful for understanding the physics of gravitational collapse, but they are not well suited to a detailed comparison with observations since they do not have realistic boundary conditions.

In contrast to the high mass infall rate measured in the IRAS 4A envelope, the spontaneous collapse of the very young Class 0 protostar IRAM 04191 in the Taurus molecular cloud is much less vigorous with a mass infall rate of only $2 \times \frac{c_s^3}{G}$ (see Belloche et al. 2002). This could explain the order of magnitude difference between the bolometric luminosities of the two protostars that have approximately the same age since the beginning of the main accretion phase (see Lesaffre et al. 2005).

5.2. Origin of the external compression

The N_2H^+(1–0) maps of Fig. 5 show that the material emitting at "blueshifted" velocities is displaced toward the South-West with respect to the material emitting at "redshifted" velocities and that both components have the same shell-like morphology at the edge of cavity 2 of Lefloch et al. (1998) seen in maps of continuum emission (see also Sandell & Knee 2001; Hatchell et al. 2005). We interpret the velocity difference between the two components as the result of "inward" motions and conclude that the "blueshifted" material is in the background and moving toward the "redshifted" material along a direction projected onto the plane of the sky at PA $\sim 45°$ in the IRAS 4 region and PA $\sim 0°$ in the SVS13/VLA 12 region. This geometry and this velocity structure remind us of an expanding shell, the center of which would be located in the background and southwest of NGC 1333. The "blueshifted" component would be the expanding shell itself while the "redshifted" component would be the ambient medium. In this scenario, the whole region around IRAS 4 and IRAS 2 should show signatures of "inward" motion, i.e. the motion of the "blueshifted" component toward the "redshifted" component. This might indeed be the case since Walsh et al. (2006) claim that they have detected "global infall" in this region. On smaller scales in the IRAS 4A region, this scenario also fits, from a kinematical point of view, into the framework of the collapse model we investigated in Sect. 4. The external perturbation triggering the collapse of the dense core would then be the impact of this expanding shell on the ambient medium.

In this scenario, the origin of the external perturbation should be located in the background and southwest of the IRAS 4/SVS13 region. The perturbation could result from the expansion of an H II region, from a stellar wind, or from a protostellar outflow. A nearby bright star in the South-West is required for the first two assumptions. The star BD +30°547, with a spectral type between A 6 V and B 7 V (Aspin 2003, , although Cernis 1990 found a type G 2 IV), would be the best candidate. However, Preibisch (2003) finds with XMM-Newton that this star is in the foreground, so in our scenario, it cannot be the origin of the external perturbation in the IRAS 4 region. Since NGC 1333 is filled with many outflows (Knee & Sandell 2000), the collapse of IRAS 4 could have been triggered by one of them. Like Hennebelle et al. (2003), Motoyama & Yoshida (2003) numerically investigated the collapse of dense cores triggered by an external perturbation. They initiated the collapse by setting a nonzero inward velocity at the boundary of the dense core and found that the maximum value of the mass infall rate is proportional to the momentum given to the dense core by the external perturbation and, in particular, that an input momentum of $\sim 0.1\ M_\odot$ km s^{-1} yields a mass infall rate of $\sim 1 \times 10^{-4}\ M_\odot$ yr^{-1}. The collapse of IRAS 4A could thus have been started by an

external perturbation with a momentum of ~0.1 $M_\odot$ km s^{-1}. This is a typical value for the present molecular outflows in NGC 1333 (Knee & Sandell 2000). The shock created by a present or former outflow could therefore have triggered, directly or indirectly, the collapse of IRAS 4A. This would fit the scenario of shock-driven sequential star formation put forward by Warin et al. (1996) for NGC 1333. Indeed, the cavity in the South-West of IRAS 4A could be the relic of a former outflow (see Quillen et al. 2005). However, we have not yet found a good protostellar candidate that could have been the origin of such an outflow in the South-West.

We mentioned the limitation of our 1D spherical modeling for IRAS 4A in Sect. 4.3 and suggested an asymmetry of the source along the line of sight, the rear hemisphere being denser than the front hemisphere. This asymmetry could stem from the fast external compression itself, which is unlikely to be isotropic on the scale of the IRAS 4A envelope. Boss (1995) showed examples of such asymmetries in dense cores set in collapse by a shock wave hitting only one hemisphere (see his Fig. 2). It would be geometrically consistent with the idea that the compression wave that triggered the collapse of the IRAS 4A envelope is coming from the back, as deduced above from the morphology and kinematics of the N_2H^+(1–0) maps.

5.3. Non uniform turbulence

We found in Sect. 4.3 that the non-thermal line broadening, which is likely to stem from turbulent motions, decreases toward the center of IRAS 4A from supersonic to subsonic velocities by nearly a factor of 3. A similar conclusion has already been drawn by Di Francesco et al. (2001) based on their N_2H^+ interferometric data. The turbulence is thus supersonic in the outer parts of the IRAS 4A envelope but only subsonic in the inner dense region. The subsonic turbulence in the inner part of the envelope is reminiscent of the low level of turbulence found in prestellar condensations (e.g. in the ρ Oph protocluster, see Belloche et al. 2001). It could then indicate the conditions prevailing in the dense core before the onset of collapse. In the outer parts of the envelope, the supersonic turbulence $\sigma_{\rm NT} \sim 0.50$ km s^{-1}, which we derived from the CS self-absorption, is nearly as large as the amplitude of the non-thermal motions deduced by Warin et al. (1996) from the low density tracer $C^{18}O$(1–0) in the molecular cloud (see also Fig. 7 of Quillen et al. 2005, for $C^{18}O$ data with a better spatial resolution). The outer parts of the IRAS 4A envelope are therefore affected by the supersonic turbulence that permeates the whole cloud and that may have been powered by the numerous outflows located in NGC 1333 (Quillen et al. 2005). In the scenario we proposed in Sect. 5.2, the supersonic turbulence could have been generated in the outer parts of the IRAS 4A envelope by the expansion of the southwestern cavity.

5.4. Rotation and binary formation

Detecting rotation and measuring its magnitude in the envelope of IRAS 4A is not straightforward. We mentioned in Sect. 3.4 that the blue component of the low-optical-depth tracers shows a velocity gradient of ~9.7 km s^{-1} pc^{-1} at PA ~ 38° over ~40″, which is on the same order as the gradient measured in IRAM 04191 that we interpreted as rotation (Belloche et al. 2002). However, there are two caveats for IRAS 4A. First, the double-peaked structure of our single-dish low-optical-depth spectra makes the analysis difficult in terms of rotation. Second, Di Francesco et al. (2001) observed N_2H^+(1–0) with PdBI and measured centroid velocity differences of about 0.5–1 km s^{-1} over ~12″, which corresponds to a velocity gradient of ~30–50 km s^{-1} pc^{-1}, at a position angle PA ~ 135°. Their position angle was only a rough estimate and a fit to their centroid velocity map would give a position angle probably close to 90° (see their Fig. 2b), but this is still ~50° away from our single-dish measurement so it is unclear whether these velocity gradients trace indeed rotation.

However, if we assume that the velocity gradient we measured in Sect. 3.4 is a good estimate of the amount of rotation in the envelope and suppose at first order that it is a solid-body rotation, then we find a ratio of rotation energy over gravitational energy of $\beta \sim 0.02$. This is similar to the conditions investigated by Hennebelle et al. (2004) when studying the fragmentation process in a rotating core set in collapse by a fast external compression. Their main conclusion was that a fast compression promotes fragmentation and the formation of multiple protostars. With a very rapid compression ($\phi = 0.1$), they show that this process occurs through the formation of a ring which becomes unstable very quickly. It breaks up into several pieces that, in their example, merge into two protostars. For their simulation with a dense core of 1 $M_\odot$, the proto-binary separation is about 140 AU (see their Fig. 7), which corresponds to 840 AU if we normalize their model to the mass of the IRAS 4A envelope (6 $M_\odot$). IRAS 4A is indeed a binary system with a separation of 1.8″, i.e. 570 AU at a distance of 318 pc (see Looney et al. 2000; Reipurth et al. 2002). It is therefore tempting to conclude that the formation of the IRAS 4A binary system results from the fast external compression that triggered the collapse of the dense core.

5.5. Collapse of NGC1333 IRAS 4B

As for IRAS 4A, Di Francesco et al. (2001) find an inverse P-Cygni profile toward the Class 0 protostar IRAS 4B (Sandell et al. 1991). They conclude that it is also collapsing, with a similar mass infall rate of 3.7×10^{-5} $M_\odot$ yr^{-1}. Since it lies along the same N_2H^+ filament as IRAS 4A (see Fig. 5) and is in a similar evolutionary stage, we suggest that the gravitational collapse of its envelope was triggered by the same external perturbation, the expanding shell suggested in Sect. 5.2.

We note that IRAS 4B is an 11″ binary and possibly a system with even higher multiplicity (see Lay et al. 1995; Looney et al. 2000). However, the main companion was not detected in continuum emission at 3.6 cm by Reipurth et al. (2002) and is probably much more evolved than the primary (Looney et al. 2000). This raises the question of whether it really belongs to the IRAS 4B system or is physically unrelated and appears close to the Class 0 protostar in the plane of the sky just by chance.

5.6. Alternative interpretations?

In the past, it has been claimed that the NGC 1333 molecular cloud includes several independent velocity components seen in emission and/or absorption (see Langer et al. 1996; Choi 2001; Choi et al. 2004). In particular, Choi et al. (2004) reject the infall interpretation of Di Francesco et al. (2001) and instead propose a foreground absorbing layer at 8 km s^{-1} that is physically unrelated to IRAS 4A. They assume a very low systemic velocity of 6.7 km s^{-1} for IRAS 4A, yielding highly redshifted absorption dips in the optically thick spectra, and argue that standard collapse models like the inside-out collapse model (Shu 1977) would never produce such highly redshifted dips given the age

of the protostar, and that the faster Larson-Penston model would produce linewidths that are much too broad to fit these highly redshifted dips. However, the model presented in Sect. 4 shows that a systemic velocity of 7.2 km s^{-1} and a collapse induced by a fast external compression can fit both the optically thick and thin lines reasonably well. The fit to our data set does not require any additional absorbing layer that is physically unrelated to IRAS 4A, as claimed by Choi et al. (2004). Our scenario, which requires only one source, is simpler. Therefore we think it is more likely.

6. Summary and conclusions

We have carried out a detailed analysis of the physical structure of the envelope of the Class 0 protostar IRAS 4A in the NGC 1333 molecular cloud. Our main results and conclusions are as follows:

1. The density profile deduced from previous interferometric and single-dish millimeter continuum measurements is steep (p = 2.3), and the envelope is much denser than a singular isothermal sphere at 10 K.
2. Our new set of molecular line data obtained with the IRAM 30 m telescope shows the classical spectroscopic signature of collapse with absorption dips of optically thick lines redshifted by 0.5 km s^{-1} with respect to the systemic velocity of the source traced by optically thin lines.
3. Both the density structure deduced from the continuum observations and our set of CS, $C^{34}S$, and N_2H^+ spectra can be well fitted by a model of collapse induced by a fast external compression with a time of 1–2$\times10^4$ yr after the formation of the central protostar. This age is consistent with the lifetime estimated for Class 0 protostars.
4. We deduce a very high mass infall rate of 0.7–2 $\times$ 10^{-4} $M_\odot$ yr^{-1} in the envelope of IRAS 4A. It results from both the overdensity and the high velocities generated by the fast external compression.
5. Our radiative transfer modeling reveals a strong decrease in the level of turbulence from supersonic velocities in the outer regions to subsonic velocities near the center of the IRAS 4A envelope. The subsonic turbulence is probably a relic of the conditions prevailing in the dense core before the onset of collapse.
6. We found indications of the presence of an expanding shell in the vicinity of IRAS 4A, which could be the origin of the compression. This expanding shell could have simultaneously triggered the collapse of the nearby Class 0 protostar IRAS 4B. However, we did not find any evidence of a nearby bright star that could have initiated this compression through the expansion of an H II region or through a strong wind. On the other hand, the collapse of IRAS 4A and IRAS 4B could have been triggered, directly or indirectly, by an outflow, but we have not found a good protostellar candidate yet.

Acknowledgements. We would like to thank Jennifer Hatchell for her help with the software SPECX and Holger Müller for the new HCO^+ entry in the CDMS database. We also thank the referee, Mario Tafalla, for helpful comments.

References

André, P., Ward-Thompson, D., & Barsony, M. 1993, ApJ, 406, 122
André, P., Ward-Thompson,D., & Barsony, M. 2000, in Protostars and planets IV, ed. V. Mannings, A. Boss, & S. Russell (Tucson: Univ. Arizona Press), 59
André, P., Belloche, A., Hennebelle, P., & Ward-Thompson, D. 2004, Baltic Astronomy, 13, 392
Aspin, C. 2003, AJ, 125, 1480
Belloche, A., & André, P. 2004, A&A, 419, L35
Belloche, A., André, P., & Motte, F. 2001, From Darkness to Light: Origin and Evolution of Young Stellar Clusters, ASP Conf. Ser., 243, 313
Belloche, A., André, P., Despois, D., & Blinder, S. 2002, A&A, 393, 927
Blake, G. A., Sandell, G., van Dishoeck, E. F., et al. 1995, ApJ, 441, 689
Blinder, S. 1997, Thesis, Université de Bordeaux I
Bonnor, W. B. 1956, MNRAS, 116, 351
Boss, A. P. 1995, ApJ, 439, 224
Buisson, G., Desbats, L., Duvert, G., et al. 2002, CLASS manual, version 4.0 (IRAM)
Caselli, P., & Dore, L. 2005, A&A, 433, 1145
Caselli, P., Walmsley, C. M., Zucconi, A., et al. 2002, ApJ, 565, 331
Cernis, K. 1990, Ap&SS, 166, 315
Choi, M. 2001, ApJ, 553, 219
Choi, M. 2005, ApJ, 630, 976
Choi, M., Kamazaki, T., Tatematsu, K., & Panis, J.-F. 2004, ApJ, 617, 1157
de Zeeuw, P. T., Hoogerwerf, R., de Bruijne, J. H. J., Brown, A. G. A., & Blaauw, A. 1999, AJ, 117, 354
Di Francesco, J., Myers, P. C., Wilner, D. J., Ohashi, N., & Mardones, D. 2001, ApJ, 562, 770
Dore, L., Caselli, P., Beninati, S., et al. 2004, A&A, 413, 1177
Evans, N. J. II 1999, ARA&A, 37, 311
Fatuzzo, M., Adams, F. C., & Myers, P. C. 2004, ApJ, 615, 813
Flower, D. R. 1999, MNRAS, 305, 651
Getman, K. V., Feigelson, E. D., Townsley, L., et al. 2002, ApJ, 575, 354
Gottlieb, C. A., Myers, P. C., & Thaddeus, P. 2003, ApJ, 588, 655
Gregersen, E. M., Evans, N. J., Zhou, S., & Choi, M. 1997, ApJ, 484, 256
Hatchell, J., Richer, J. S., Fuller, G. A., et al. 2005, A&A, 440, 151
Hennebelle, P., Whitworth, A. P., Gladwin, P. P., & André, P. 2003, MNRAS, 340, 870
Hennebelle, P., Whitworth, A. P., Cha, S.-H., & Goodwin, S. P. 2004, MNRAS, 348, 687
Hildebrand, R. H. 1983, QJRAS, 24, 267
Hunter, C. 1977, ApJ, 218, 834
Knee, L. B. G., & Sandell, G. 2000, A&A, 361, 671
Lada, C. J., & Lada, E. A. 2003, ARA&A, 41, 57
Lada, C. J., Alves, J., & Lada, E. A. 1996, AJ, 111, 1964
Langer, W. D., Castets, A., & Lefloch, B. 1996, ApJ, 471, L111
Larson, R. B. 1969, MNRAS, 145, 271
Lay, O. P., Carlstrom, J. E., & Hills, R. E. 1995, ApJ, 452, L73
Lefloch, B., Castets, A., Cernicharo, J., Langer, W. D., & Zylka, R. 1998, A&A, 334, 269
Lesaffre, P., Belloche, A., Chièze, J.-P., & André, P. 2005, A&A, 443, 961
Looney, L. W., Mundy, L. G., & Welch, W. J. 2000, ApJ, 529, 477
Looney, L. W., Mundy, L. G., & Welch, W. J. 2003, ApJ, 592, 255
Mardones, D., Myers, P. C., Tafalla, M., et al. 1997, ApJ, 489, 719
Maret, S., Ceccarelli, C., Caux, E., et al. 2004, A&A, 416, 577
Matthews, H., & Jenness, T. 1997, Specx Cookbook Reduction of millimetre wave data, Starlink Document sc8
Motoyama, K., & Yoshida, T. 2003, MNRAS, 344, 461
Motte, F., & André, P. 2001, A&A, 365, 440
Müller, H. S. P., Schlöder, F., Stutzki, J., & Winnewisser, G. 2005, J. Mol. Struct., 742, 215
Myers, P. C., Evans, N. J. II, & Ohashi, N. 2000, in Protostars and planets IV, ed. V. Mannings, A. Boss, & S. Russell (Tucson: Univ. Arizona Press), 217
Onishi, T., Mizuno, A., & Fukui, Y. 1999, PASJ, 51, 257
Padman, R. 1993, SPECX Users' Manual, Version 6.3
Penston, M. V. 1969, MNRAS, 144, 425
Preibisch, T. 2003, A&A, 401, 543
Quillen, A. C., Thorndike, S. L., Cunningham, A., et al. 2005, ApJ, 632, 941
Reipurth, B., Rodríguez, L. F., Anglada, G., & Bally, J. 2002, AJ, 124, 1045
Sandell, G., & Knee, L. B. G. 2001, ApJ, 546, L49
Sandell, G., Aspin, C., Duncan, W. D., Russell, A. P. G., & Robson, E. I. 1991, ApJ, 376, L17
Schmid-Burgk, J., Muders, D., Müller, H. S. P., & Brupbacher-Gatehouse, B. 2004, A&A, 419, 949
Shu, F. H. 1977, ApJ, 214, 488
Shu, F. H., Adams, F. C., & Lizano, S. 1987, ARA&A, 25, 23
Smith, K. W., Bonnell, I. A., Emerson, J. P., & Jenness, T. 2000, MNRAS, 319, 991
Tafalla, M., Mardones, D., Myers, P. C., et al. 1998, ApJ, 504, 900
Terebey, S., Chandler, C. J., & André, P. 1993, ApJ, 414, 759
Walsh, A. J., Bourke, T. L., & Myers, P. C. 2006, ApJ, 637, 860
Warin, S., Castets, A., Langer, W. D., Wilson, R. W., & Pagani, L. 1996, A&A, 306, 935
Whitworth, A., & Summers, D. 1985, MNRAS, 214, 1